Check for updates

ADVANCED MATERIALS
www.advmat.de

A Ceramic-Electrolyte Glucose Fuel Cell for Implantable Electronics

*Philipp Simons, Steven A. Schenk, Marco A. Gysel, Lorenz F. Olbrich, and Jennifer L. M. Rupp**

Next-generation implantable devices such as sensors, drug-delivery systems, and electroceuticals require efficient, reliable, and highly miniaturized power sources. Existing power sources such as the Li–I_2 pacemaker battery exhibit limited scale-down potential without sacrificing capacity, and therefore, alternatives are needed to power miniaturized implants. This work shows that ceramic electrolytes can be used in potentially implantable glucose fuel cells with unprecedented miniaturization. Specifically, a ceramic glucose fuel cell—based on the proton-conducting electrolyte ceria—that is composed of a freestanding membrane of thickness below 400 nm and fully integrated into silicon for easy integration into bioelectronics is demonstrated. In contrast to polymeric membranes, all materials used are highly temperature stable, making thermal sterilization for implantation trivial. A peak power density of 43 µW cm^{-2}, and an unusually high statistical verification of successful fabrication and electrochemical function across 150 devices for open-circuit voltage and 12 devices for power density, enabled by a specifically designed testing apparatus and protocol, is demonstrated. The findings demonstrate that ceramic-based micro-glucose-fuel-cells constitute the smallest potentially implantable power sources to date and are viable options to power the next generation of highly miniaturized implantable medical devices.

1. Introduction

Implantable medicine is undergoing a fundamental paradigm shift from passive to active implants such as electronic devices that sense and augment human health and body functions. These new biomedical implantable devices range from drug-delivery systems and sensors to electroceuticals and bioelectronic devices. In particular, electroceuticals and neurostimulation are a rapidly growing market with an annual growth rate of 8.5% and an estimated expected global market volume of US$ 41 billion in 2027,[1] with global medical technology companies as well as start-ups seeking to commercialize technology.[2,3] To drive this revolution in implantable medicine, new power sources are required that can deliver safe and stable energy to implants while enabling the miniaturization of these devices to an unprecedented scale to minimize the impact of implants on patients. Power requirements for implantable devices typically lie in the range of 100 nW to 1 mW,[4–6] and power sources with increased energy and power density beyond current capabilities could enable new functionalities in sensing, electronic stimulation, or drug delivery that are currently unattainable.

To date, implantable devices are primarily powered by batteries such as the Li–I_2 pacemaker battery[7,8] with volumetric and gravimetric energy densities of ≈1000 Wh L^{1} and ≈270 Wh kg^{1},[9] respectively, or through wireless energy transmission such as RF transmission[10,11] or ultrasound.[12] Because of their nature, batteries cannot be easily miniaturized without sacrificing substantial energy storage capacity,[13] and because power transferred via induction scales with the area of the antenna, the miniaturization potential of wireless energy transfer is also limited. In addition, the Li–I_2 pacemaker battery is a non-rechargeable cell, which means that

P. Simons, S. A. Schenk, M. A. Gysel, L. F. Olbrich, J. L. M. Rupp
Department of Materials Science and Engineering
Massachusetts Institute of Technology
77 Massachusetts Avenue, Cambridge, MA 02139, USA
E-mail: jrupp@mit.edu

The ORCID identification number(s) for the author(s) of this article can be found under https://doi.org/10.1002/adma.202109075.

© 2022 The Authors. Advanced Materials published by Wiley-VCH GmbH. This is an open access article under the terms of the Creative Commons Attribution-NonCommercial-NoDerivs License, which permits use and distribution in any medium, provided the original work is properly cited, the use is non-commercial and no modifications or adaptations are made.

DOI: 10.1002/adma.202109075

S. A. Schenk
Department of Mechanical Engineering
EPFL
Station 9, Lausanne 1015, Switzerland

M. A. Gysel
Department of Mechanical and Process Engineering
ETH Zürich
Leonhardstrasse 21, Zürich 8092, Switzerland

L. F. Olbrich
Department of Chemistry and Applied Biosciences
ETH Zürich
Vladimir-Prelog Weg 1–5, Zürich 8093, Switzerland

J. L. M. Rupp
Department of Electrical Engineering and Computer Science
Massachusetts Institute of Technology
77 Massachusetts Avenue, Cambridge, MA 02139, USA

replacement surgery is required once the energy in the battery is depleted, creating a risk for complications. Because of these limitations, alternative implantable energy-harvesting solutions with the prospect of higher energy density and degree of miniaturization are being researched, bringing glucose fuel cells[14–16] as well as thermoelectric,[17,18] piezoelectric,[19,20] and triboelectric generators[21,22] into focus.

Compared with batteries, glucose fuel cells allow for significant volumetric scale-down because they do not physically store energy but instead directly convert fuel that is readily available inside the body into electrical energy. Considering also the practical implantation, glucose fuel cells can operate and harvest energy essentially anywhere in the body. For instance, polymer-electrolyte glucose fuel cells can utilize a wide range of body fluids such as interstitial fluid,[14] the bloodstream,[14] tears,[23] or cerebrospinal fluid.[24] In contrast, thermoelectric generators require temperature gradients, which are very small inside the body, and piezoelectric and triboelectric generators require kinetic energy, which limits applicability to moving organs or body parts. Therefore, among these alternative power sources, glucose fuel cells are particularly promising candidates for next-generation implantable power sources.

To put the development of glucose fuel cells into techno-historical context, **Figure 1**a summarizes the development of implantable power sources versus key milestones of implant technology. Implantable power sources and implantable devices have continuously affected each other in their progress toward new treatments and device classes, and power sources have evolved with steady improvement of energy storage/conversion performance metrics and miniaturization. In 1960, the first pacemaker, powered by a zinc mercuric oxide primary battery, was implanted into a human,[25] and in addition to revolutionizing the treatment of cardiac diseases, this invention galvanized the development of implant technology across all fields of medicine while also motivating research on new implantable power sources for these implant technologies. Only shortly after, in 1964, the first abiotic[26] and enzymatic[27] polymer-electrolyte glucose fuel cells were invented, which were motivated by the need to power new implant classes such as the pacemaker. However, when the Li–I_2 pacemaker battery was invented in 1971,[8] this disruptive power source became the dominant source of energy for implantable devices, causing research into alternative implantable power sources to fall largely dormant for decades. During the 1980s and 1990s, new treatments such as implantable drug delivery and neural stimulation evolved, and implant technology continued to follow macro-trends such as interfacing between the human body and electronic devices as well as steady miniaturization. With the arrival of

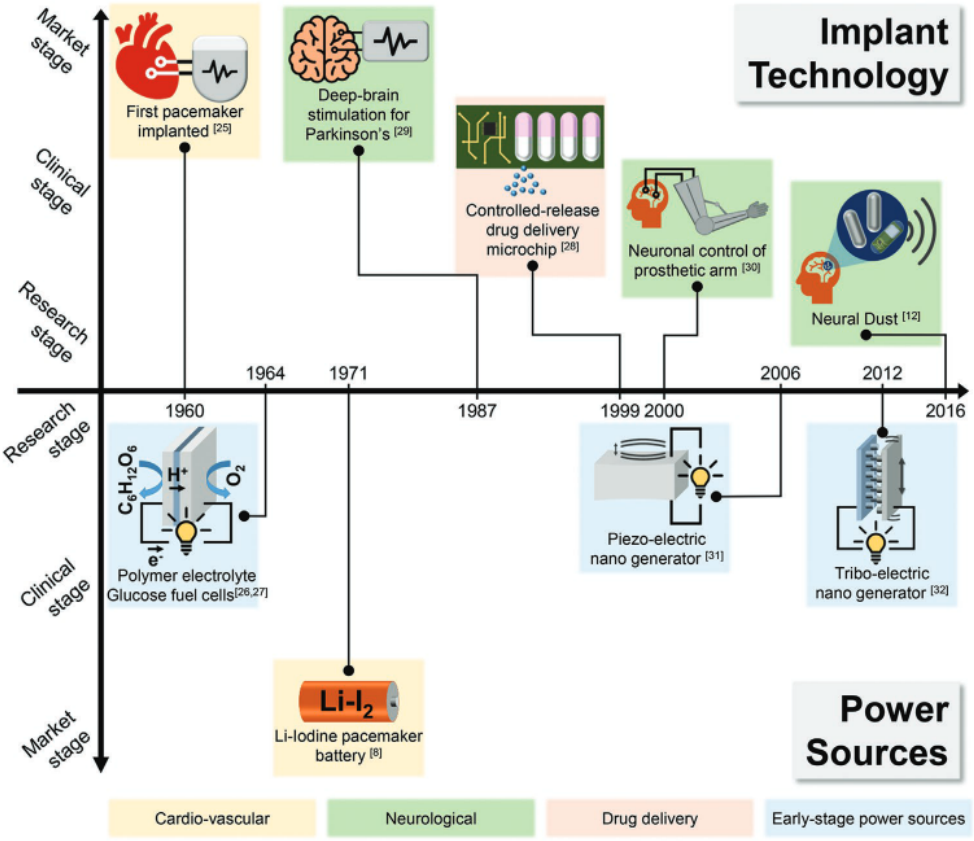

Figure 1. Techno-historical timeline of implant technology and implantable power source development.[8,12,25–32] Implantable devices and their power sources have affected each other since the 1960s. The dominant implantable power source for most established, market-stage devices to date is the Li–I_2 pacemaker battery, invented in 1971. Recent trends in implant technology include increased miniaturization and neural interfacing, sparking a new push for highly miniaturized, long-term-stable implantable power sources. New power sources, e.g., triboelectric and piezoelectric nanogenerators, aim to combine efficient energy harvesting with on-chip integration to meet the requirements of new, miniaturized implantable devices.

© 2022 The Authors. Advanced Materials published by Wiley-VCH GmbH

the fourth industrial revolution, the boundaries between the physical, digital, and biological world began to intersect, fusing new computing, sensing, and treatment capabilities. Here, a generation of new implantable device classes evolved, such as microchip-based drug-delivery systems,[28] deep-brain stimulators,[29] and neural interfaces[30] that evolved to highly miniaturized so-called neural dust.[12] This latest push for miniaturized, integrated bioelectronics has recently reignited the need for new implantable power sources with higher energy density to minimize the space requirements of implants in patients. This includes the invention of new miniaturized power generators such as the piezoelectric nanogenerator[31] and the triboelectric nano generator[32] over the last 15 years and has led to a renaissance of research in polymer-electrolyte glucose fuel cells for implantable applications.

For any implantable glucose fuel cell, a high degree of miniaturization and good electrochemical conversion efficiency are desired. To achieve these objectives, implantable glucose fuel cells commonly employ one of two catalyst classes, namely enzymatic[15] or abiotic[14,33] catalysts. Enzymatic glucose fuel cells use enzymes such as glucose oxidase to catalyze the electrode reactions, whereas their abiotic counterparts use non-biological materials such as noble metals, alloys, carbon, or composites thereof to catalyze the anodic and cathodic reactions. Enzymes exhibit very high catalytic selectivity; however, their lifetime is typically less than 30 days due to enzyme and charge-transfer degradation as well as leaching of enzymes and mediators into aqueous solution.[34,35] Abiotic glucose fuel cells, on the other hand, promise higher long-term stability and faster charge transfer than enzymatic glucose fuel cells because abiotic catalysts do not face rapid degradation or charge-transfer limitations. For the electrolyte, to date, glucose fuel cells typically rely on polymer-based proton-exchange membranes or make use of the electrolytic properties of the medium into which they are implanted (e.g., blood, interstitial fluid, cerebrospinal fluid) in a so-called membraneless configuration. Proton-exchange membranes (e.g., Nafion, poly(vinyl alcohol) PVA–poly(acrylic acid) (PAA) are well researched polymeric ion conductors with high ionic conductivities of up to 0.1 S cm^{-1} at body temperature for Nafion.[36] Despite this good conductivity, polymer-electrolyte glucose fuel cells exhibit several drawbacks as implantable power sources related to the polymer nature of the electrolyte:

i. Natural limitation for further miniaturization and increase of energy density: To avoid fuel cross-over,[37] commercial Nafion membranes require a minimum thickness of at least 25 µm (exemplified by Nafion HP,[38] the thinnest commercially available type), which creates a lower limit for miniaturization.
ii. Challenge to integrate with silicon-based chip design and microfabrication: Recent developments in integrated electronics for biomedical applications, such as microchip drug-delivery systems,[28] show that direct on-chip silicon integration of the power source can drive further miniaturization and efficiency of implantable bioelectronics. The current materials for glucose fuel cells, using polymer-based electrolytes, are not easily integrated with semiconductor manufacturing processes, making on-chip integration for such implant applications difficult.
iii. Inability for thermal sterilization: A common procedure to sterilize implants during an implantation process is to apply moist heat sterilization. Although Nafion has a high thermal stability up to 280 °C,[39] exposure to temperatures of 120 °C or more causes irreversible damage to the material, including irreversible swelling[40] and conductivity reduction,[41] damaging both the mechanical stability and electrochemical performance of the device. These effects make moist heat sterilization, a critical step for implantation that is commonly performed at 121 or 132 °C,[42] impossible.

These challenges of miniaturization, silicon on-chip integration, and thermal sterilization of current polymer-based glucose-fuel-cell types may be overcome by moving away from polymer electrolytes and, instead, developing glucose fuel cells that operate on ceramic proton-conducting electrolytes.

Ceramic materials have a long history of use as electrolytes in solid oxide fuel cells (SOFCs)[43–46] and protonic ceramic fuel cells (PCFCs)[47–51] operating on hydrogen and exhibit higher thermal, chemical, and mechanical stability than polymer electrolytes such as Nafion. However, although a wide range of proton-conducting ceramics is being researched for hydrogen PCFCs, they have not yet been considered for glucose fuel cells. Consequently, the material selection, electrochemical operation principle, and even basic proof of operation of a ceramic glucose fuel cell all remain unexplored. To select the electrolyte material for such a ceramic glucose fuel cell for implantable applications, the most fundamental criterion is that the proton-conducting ceramic must be biocompatible. This criterion excludes many of the best-performing proton-conducting ceramics such as yttria-doped barium zirconate (BZY)[51–53] and other solid solutions of barium zirconate and barium cerate because of their toxicity.[54] In contrast, low-temperature proton conductors such as ceria[55] or yttria-stabilized zirconia (YSZ)[56] are non-toxic and biocompatible; in addition, they are stable up to temperatures far in excess of 1000 °C, making thermal sterilization trivial. The proton conductivity of hydrated ceria, CeO_2, reaches up to 10^{-3} S cm^{-1} at room temperature,[57–60] which is sufficient to enable the operation of energy-conversion devices at body temperature. Furthermore, ceria is known to exhibit enzyme-like properties when structured as nanoparticles and is being actively researched for oncology applications.[55,61]

Ceria as a ceramic proton-conducting electrolyte offers a pathway to miniaturization that is particularly appealing for implantable microdevices. Ceria and its solid solutions were among the first materials to be integrated as oxygen-ion-conducting electrolytes into micro-SOFCs with electrolyte thicknesses scaled down to hundreds of nanometers and integrated on silicon chips.[43,62] A transfer of this technology toward glucose fuel cells can enable the realization of glucose-fuel-cell devices that are fully integrated on silicon with high volumetric power density given the device thickness of only a few hundreds of nanometers. This miniaturization, in combination with the thermal and mechanical robustness of ceria, opens scale-down opportunities on the sub-micrometer scale previously inaccessible to polymer-electrolyte glucose fuel cells.

There have been no reports of ceramic-based glucose fuel cells to date, and therefore, the electrochemistry as well as

© 2022 The Authors. Advanced Materials published by Wiley-VCH GmbH

potential designs, material selection, and operating principles of such devices for future implants are also unexplored. Thus, demonstrating a first design of a ceramic-based abiotic glucose fuel cell not only opens up a potential new class of power sources for future implantable devices but also paves the way to overcome the limitations of existing polymer-based glucose fuel cells through miniaturization, on-chip integration, and the ability for thermal sterilization. Ultimately, this is a step toward enabling fully integrated and miniaturized implants, following the fast-paced evolution of microchip devices such as drug-delivery systems and neural dust as well as toward future electroceuticals and miniature bioelectronics. In this work, we present a glucose fuel cell that is fabricated entirely from solid-state materials, such as ceramics and noble metals. The use of ceria as the ceramic proton-conducting electrolyte overcomes many of the shortcomings of polymer-based electrolytes, and the entire glucose fuel cell is fabricated on a silicon chip using standard semiconductor microfabrication techniques, which means that the fuel cell can be easily and directly integrated into bioelectronic devices and implants. We demonstrate the principle and operation of the ceramic-based miniaturized glucose fuel cell and explore the operating mechanism and electrochemical processes for glucose conversion. Eventually, our findings could guide efforts toward new power source alternatives for implants particularly suited for a high degree of miniaturization and on-chip integration beyond batteries.

2. Results and Discussion

A promising strategy to develop glucose fuel cells with on-chip integration is to design a manufacturing route based on thin-film technology. We select CeO_2 as the proton-conducting electrolyte and platinum films as the electrodes, serving both as catalysts and current collectors. The proton-conducting ceria was fabricated as free-standing fuel-cell membranes on a silicon chip, and optimal processing conditions were determined to establish a proof of concept for a ceramic glucose micro-fuel-cell and characterize its electrochemistry and performance.

2.1. Ceramic-Based Glucose Fuel Cell Design and Electrochemical Operational Principle

The design of this ceramic-based glucose fuel cell consists of a proton-conducting electrolyte, ceria, and porous platinum electrode films for the conversion of glucose and oxygen, respectively. For the proof-of-concept, we designed the glucose fuel cell in a two-chamber operation architecture, which enabled the separation of glucose and oxygen at the two electrode sides (see **Figure 2**a). This architecture is well suited for the proof-of-concept of the reaction chemistry at both electrodes. A key challenge in the design and fabrication of such micro-glucose-fuel-cells based on ceramics is to create crack-free, self-supported freestanding membrane systems consisting of a Pt anode/CeO_2 electrolyte/Pt cathode at length scales on the order of only a few hundred nanometers. We demonstrate the successful fabrication of 30 individual crack-free glucose fuel cells on a silicon chip (Figure 2b,c), throughout five different glucose fuel cells, resulting in 150 visually intact glucose fuel cells. Each glucose fuel cell was 370 ± 40 nm thin and measured 300 µm × 300 µm in area. Given the degree of miniaturization of the electrolyte, these ceramic glucose fuel cells were two-orders-of-magnitude thinner than commercial Nafion, directly translating into a smaller device footprint for future patients.

For actual implantation, these glucose fuel cells would operate under physiological levels of glucose concentration, which varies by location and body fluid, ranging from 3.9 to 6.7×10^{-3} M for blood,[63] 3 to 4×10^{-3} M for interstitial fluid,[64] and 2.5 to 4.4×10^{-3} M for cerebrospinal fluid.[65] The electrochemical operation principle of the ceramic micro-glucose-fuel-cell is such that at the anode, glucose ($C_6H_{12}O_6$) is oxidized to form gluconic acid ($C_6H_{12}O_7$) and thereby releases protons and electrons in the anodic reaction step:

$$\text{Anode reaction: } C_6H_{12}O_6 + H_2O \rightarrow C_6H_{12}O_7 + 2H^+ + 2e^- \quad (1)$$

The protons then travel through the proton-conducting electrolyte and reach the cathode, where they react with oxygen and electrons in the cathodic reaction step to form water:

$$\text{Cathode reaction: } \frac{1}{2}O_2 + 2H^+ + 2e^- \rightarrow H_2O \quad (2)$$

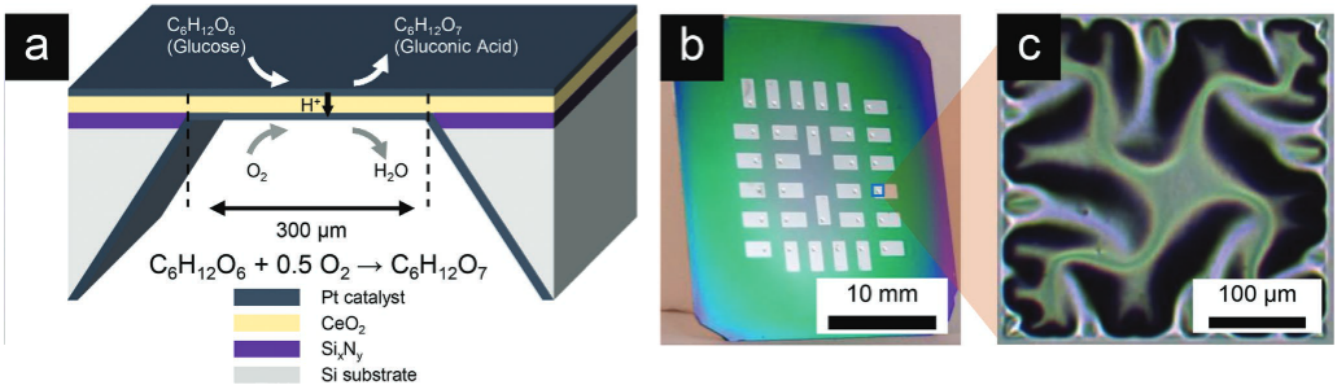

Figure 2. Schematic of glucose fuel cell, chip, and individual device. a) Schematic of a ceramic glucose fuel cell based on a freestanding membrane of a porous Pt anode/CeO_2 electrolyte/dense Pt cathode. b) Optical photograph of fuel-cell chip containing 30 individual glucose-fuel-cell devices. c) Optical microscopy image of an individual freestanding ceria membrane.

© 2022 The Authors. Advanced Materials published by Wiley-VCH GmbH

The overall electrochemical reaction of the glucose fuel cell is given by

$$\text{Glucose fuel cell reaction: } C_6H_{12}O_6 + \frac{1}{2}O_2 \rightarrow C_6H_{12}O_7 \quad (3)$$

The electrons travel through an external circuit between the anode and cathode and can thereby power an implantable device. The Gibbs free energy of the overall glucose-fuel-cell reaction (Equation (3)), i.e., the reaction of glucose with oxygen to form gluconic acid, is $\Delta G^0 = -2.51 \times 10^5$ J mol^{-1}, which results in an equilibrium Nernst potential of $U^0 = 1.08$ V.[66]

2.2. Designing Ceramic Glucose-Fuel-Cell Functional Components with High Degree of Miniaturization

To successfully assemble the ceramic glucose fuel cell on silicon and operate it in liquid glucose solution, it is necessary to balance a range of properties including high mechanical stability, low chemical cross-talk between electrodes, high proton conductivity of the electrolyte, and high catalytic activity of the electrodes. All these properties need to be optimized to achieve operation under a potential as close as possible to the theoretical Nernst potential of the fuel cell. To balance these requirements at the electrolyte component, we fabricated two different microstructures of the ceria solid proton-conducting electrolyte: a dense, columnar microstructure, depicted schematically in the left half of **Figure 3**b and in SEM images in Figure 3c,d, and a cauliflower-like rough microstructure, depicted schematically in the right half of Figure 3a and in SEM images in Figure 3e,f.

The dense, columnar microstructure resembles that typically used in micro-SOFCs[62] and prioritizes the blocking of chemical cross-talk between the electrodes. The SEM images confirm the successful growth of dense, columnar ceria, both in the top view (Figure 3c) and cross-sectional view (Figure 3d). The diameter of these columnar grains lies between 10 and 50 nm, as seen in the SEM image. The rough microstructure serves two main purposes. First, this rough microstructure is designed to enhance the overall proton conductivity of the electrolyte through the rough, high-surface-area configuration of ceria, allowing water to fill the open porosity. This design was based on earlier findings that proton conduction in ceria is enhanced along the surface of hydrated ceria.[57] Second, this rough microstructure reduces the mechanical stress state in the fuel-cell membrane compared with that in fully dense films, increasing the mechanical stability and robustness of the fabrication process (see Figure S2, Supporting Information). The rough microstructure is designed such that at the bottom, the film is dense with a base thickness of approximately 20 nm, and above this fully dense microstructure region, it exhibits a disordered, cauliflower-like microstructure; see schematic and SEM image in Figure 3b,f. Similar to the fully dense electrolyte configuration, the dense section of the rough-electrolyte configuration serves as a blocking layer for the liquid glucose-containing fuel to avoid any chemical or ionic short-circuiting through water. Overall, the rough ceria electrolyte microstructure has a relatively short dense microstructural cross-section, with the goal being to increase the overall effective proton conductivity as well as to increase the protonic transference number of the electrolyte. The overall rough and disordered microstructure can be seen in both the surface and top-view SEM images (Figure 3e,f). The grain size varies strongly throughout the disordered ceria film, with approximate grain sizes between 1 and 50 nm, and the RMS surface roughness was estimated to be 30 nm from the SEM images. To control the microstructure of the ceria electrolyte, we selected suitable pulsed laser deposition (PLD) parameters based on earlier findings that below a critical deposition pressure of ≈0.05 mbar, ceria thin films deposited via PLD are fully dense, whereas above this pressure, they exhibit a rough microstructure.[67] The PLD depositions were optimized to achieve the desired microstructures on substrate-supported samples before fabrication of full glucose-fuel-cell devices. The cubic fluorite structure of the ceria proton-conducting electrolyte was confirmed by XRD and Raman spectroscopy analysis, as discussed in more detail in the Supporting Information, and is in good agreement with the literature.[68] Because all samples are stored at ambient oxygen concentration and room temperature after the PLD deposition, it is assumed that the ceria is fully stoichiometric.

The electrodes were designed to achieve high catalytic activity and selectivity. The anode, being the top electrode of the glucose fuel cell, was fabricated as a layer of nanoporous platinum with a thickness of 100 nm. Porous platinum was selected as the anode catalyst because Raney-type nanoporous platinum is known to be a selective catalyst for the oxidation of glucose in the presence of oxygen.[69,70] We developed a reactive-sputtering fabrication route to obtain de-alloyed porous platinum rather than using the Raney-type route used previously for polymeric glucose fuel cells that relies on chemical etching. The reactive sputtering route was selected because it is a mechanically robust process without harsh chemical etchants. This fabrication route was adapted from Jung et al.,[71] and it does not require a chemically aggressive wet-etching step, making it compatible with ceria[72,73] and a wide range of other ceramic and CMOS materials and deposition techniques. Figure 3g,h presents SEM images of the Pt anode at different magnifications. The Pt electrode was nanoporous, with a typical pore diameter of ≈100 nm. The cathode, i.e., the bottom electrode of the glucose-fuel-cell design, consisted of a dense layer of Pt serving as the catalyst for the oxygen reduction reaction (ORR). The ORR is diffusion limited, whereas glucose oxidation is kinetically, i.e., surface limited, and thus, the low-surface-area, dense Pt film at the cathode forms a selective ORR catalyst in the presence of glucose.[74] Overall, the microstructures of both electrodes were designed to enable selective catalysis of the electrode reactions, i.e., glucose oxidation and oxygen reduction, respectively.

To further clarify the microstructure and full assembly of the full ceramic glucose-fuel-cell system, Figure 3i,j presents post-mortem SEM images of a fractured fuel-cell freestanding membrane with a porous Pt top electrode, rough ceria electrolyte, and dense Pt bottom electrode. The full fuel-cell device with its functional components and a total device thickness of only 370 nm is shown. The full-device microfabrication route for the freestanding glucose-fuel-cell membrane devices consisted of a series of microfabrication steps involving photolithography, wet and dry etching, and thin-film deposition techniques. The process is described in detail in the Experimental Section and is schematically summarized in Figure S3 (Supporting

© 2022 The Authors. Advanced Materials published by Wiley-VCH GmbH

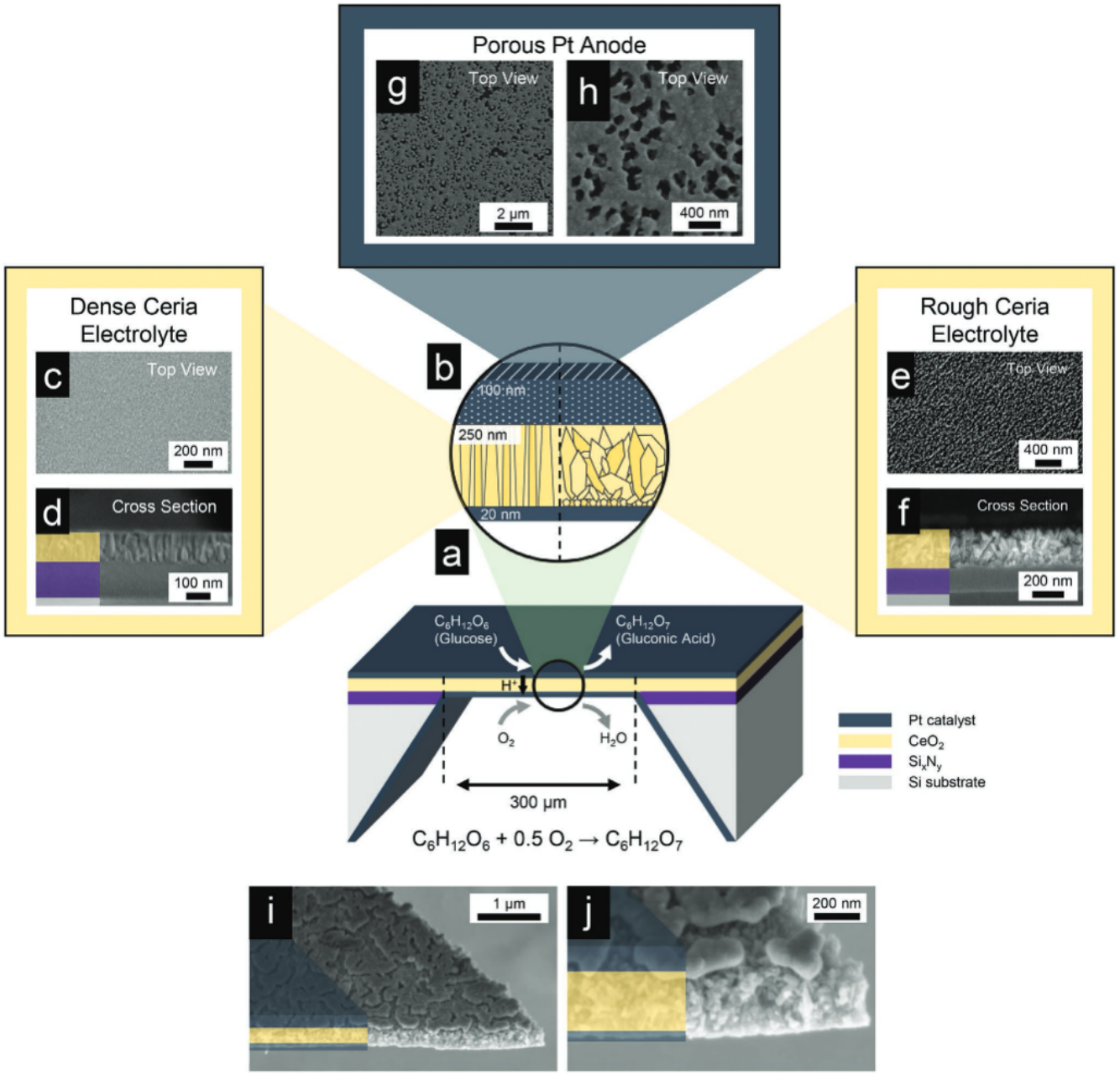

Figure 3. Schematic of ceramic glucose fuel cell and SEM analysis of its components. a,b) Schematic of ceramic glucose fuel cell consisting of free-standing ceria membrane as the proton-conducting electrolyte, a porous Pt anode, and a dense Pt cathode. b) Two different microstructures of the ceria electrolyte were employed, namely, a dense, columnar microstructure (left) and a rough, cauliflower-like microstructure (right). c) Top-view and d) cross-sectional view SEM images of the dense ceria electrolyte microstructure. e) Top-view and f) cross-sectional view SEM images of the rough ceria electrolyte microstructure. g,h) SEM images of different magnifications of the porous Pt anode. i,j) Cross-sectional SEM images at different magnifications of a full glucose fuel cell, measuring 370 nm in thickness and consisting of a porous Pt anode (top), rough ceria ceramic proton-conducting electrolyte (middle), and dense Pt cathode (bottom).

Information). The fabrication process consisting of multiple high-temperature steps above 400 °C, as well as the high thermal stability of all materials involved, indicate that the full device can be sterilized using commercial sterilization process such as steam, thermal, or chemical sterilization. All the fabrication processing steps were optimized to achieve a fabrication yield of 100% over 150 individual glucose-fuel-cell membranes, i.e., 30 membranes each on five separate silicon chips.

2.3. Overall Cell Resistance and Electrolyte Conductivity via Electrochemical Impedance Spectroscopy

Next, we analyze the electrochemical impedance of the glucose fuel cell to gain insight into the different contributions to resistance in the glucose-fuel-cell system. Electrochemical impedance spectroscopy was used to understand the sources of loss in the ceramic glucose fuel cell. We discuss here the

© 2022 The Authors. Advanced Materials published by Wiley-VCH GmbH

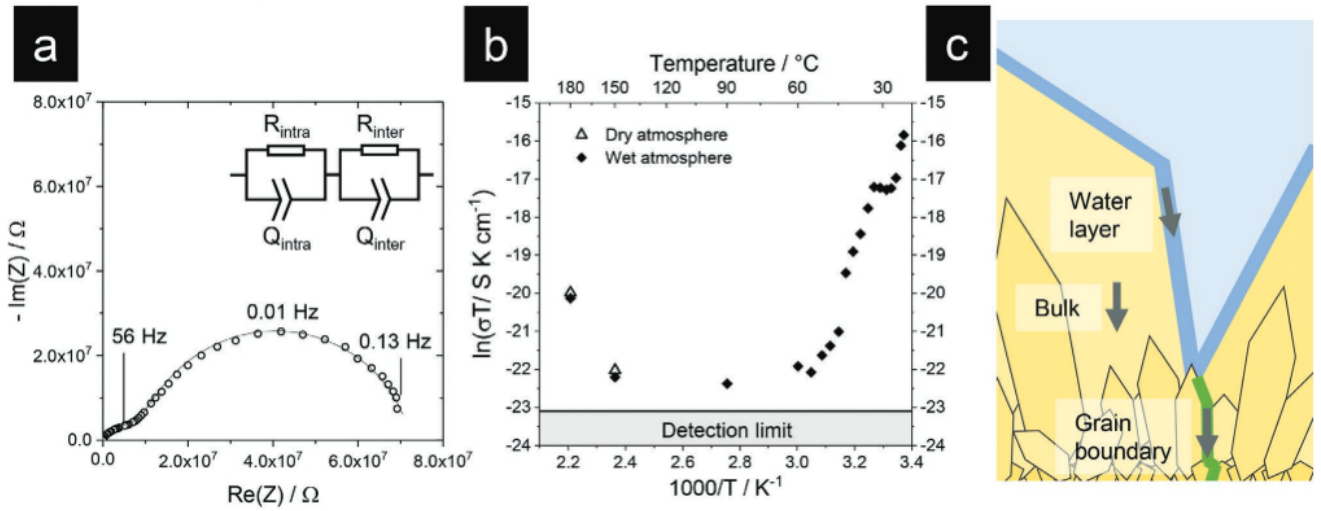

Figure 4. Impedance and proton conductivity of glucose-fuel-cell devices. a) Impedance spectrum and equivalent circuit for a glucose-fuel-cell membrane at 23.5 °C. b) Arrhenius-type plot of conductivity of the fuel-cell system extracted from EIS measurements, proving protonic conductivity at low temperatures in the hydrated case. c) Mechanism of proton conductivity through the rough ceria electrolyte structure.

exemplary case of the rough ceria electrolyte; however, the results are representative for both microstructures. **Figure 4**a presents the impedance spectrum of a glucose fuel cell with a rough microstructure taken at 23.5 °C. The entire chip was exposed to humidified air to hydrate the electrolyte. Measurements under liquid water were not possible because of the large artifacts of the water in the impedance spectra. The impedance spectrum, displayed as a Nyquist plot, contains two arcs with peak frequencies of 0.13 and 56 Hz. The two arcs are qualitatively consistent with the behavior observed for surface-limited proton conduction in porous ceria pellets,[57] which is remarkable because part of the proton transport occurred through the dense lower fraction of the ceria membrane and not along the surfaces of pores. However, the total conductivity of 5.4×10^{-10} S cm^{-1} is four-orders-of-magnitude lower than that commonly observed in surface-governed proton transport.[57,75] This difference can be explained by two factors that reduce the total conductivity. First, cross-plane proton transport through dense ceria has a higher resistance than the in-plane surface transport described by Manabe et al.;[57] in fact, in some studies, no interior contribution to proton conductivity was observed at all.[59] Here, we do observe cross-plane conductivity of which at least some fraction is occurring through the interior of the ceria membrane, i.e., which cannot be surface-limited or through an adsorbed water layer. Second, the conductivity reported is of an entire glucose-fuel-cell device, i.e., including the top and bottom electrodes and their interfaces with the ceria electrolyte. A more detailed discussion of the impedance spectrum can be found in the Supporting Information. In summary, we view this total device impedance as sufficiently low, and thus the conductivity as sufficiently high, to successfully operate as glucose fuel cells.

To further investigate the mechanism of conductivity and confirm that the observed total conductivity is in fact of protonic nature, we measured the fuel-cell impedance under wet and dry conditions and various temperatures. Confirming proton conduction and determining the device conductivity defines the electrochemical conversion efficiency and, therefore, the total power output of the ceramic glucose fuel cell. Figure 4b displays the total conductivity of the glucose-fuel-cell system with a rough electrolyte in the form of an Arrhenius-type plot under dry and humidified air. The conductivity was determined from impedance spectra measured between 22 and 180 °C for full glucose fuel cells. In the dry case, the conductivity dropped below the detection limit of the instrument below 150 °C. In contrast, for humidified air, an inflection in the conductivity was observed near 100 °C, the boiling point of water, and conductivity increased with decreasing temperature. This behavior of an apparent negative activation energy at low temperatures is typical for proton conduction in hydrated oxides such as ceria[58,60,76] and stems from the competition of thermally activated ion hopping and higher water coverage at lower temperatures. We thus confirm that proton conduction was observed and, importantly, that this occurs in a cross-plan configuration, i.e., through a dense electrolyte layer of ceria. For the rough electrolyte configuration, the vast majority of the protonic pathway through the electrolyte was governed by rough, high-surface-area ceria, as schematically depicted in Figure 4c. The water layer adsorbed to the columnar grain surface serves as a high-proton-conduction channel, with intra- and inter-grain-boundary proton conduction controlling the conductivity behavior in this region. In the bottom fraction of the electrolyte, with a thickness of roughly 20 nm, conduction occurred through dense, nanogranular ceria. Overall, we confirm proton conduction in both the rough and dense ceria microstructures of the ceria proton-conducting ceramic electrolyte, a necessary condition to operate glucose fuel cells. Based on the demonstrated proton conduction, we turned to further characterizing the function of fabricated fuel-cell devices based on both the rough and the dense electrolyte microstructures.

2.4. OCV Statistics of 150 Ceramic Glucose Fuel Cells and Power Generation Performance via *I–V* Curves

We now turn to electrochemical metrics of device operation to characterize the operation of glucose fuel cells in vitro. To

© 2022 The Authors. Advanced Materials published by Wiley-VCH GmbH

deliver a reliable proof of concept and answer the question with sufficient statistical evidence of whether a glucose fuel cell based on a ceramic proton conductor can operate, we measured the open-circuit voltage (OCV) of a total of 150 micro-fuel-cell devices under deaerated 0.5 M glucose solution in phosphate-buffered saline (PBS) solution at the anode and under air at the cathode. Among both polymeric glucose fuel cells and hydrogen-based ceramic micro-fuel-cells, this number of tested prototypes is among the highest ever reported. This large number of characterized devices was achieved by constructing a dedicated, custom-built testing setup that allows for rapid switching between individual glucose-fuel-cell devices placed on silicon chips, which formed an important basis for this work. Among the 150 glucose fuel cells measured, 120 exhibited the dense, columnar ceria electrolyte microstructure and 30 exhibited the rough electrolyte microstructure, in accordance with Figure 3. **Figure 5**a,b presents histograms of the OCVs of ceramic glucose-fuel-cell devices with dense and porous electrolyte microstructures, respectively. Figure 5c displays the apparatus used to measure the OCV of the 30 individual glucose fuel cells in rapid sequence, and additional information about the testing apparatus is provided in Figure S8 (Supporting Information). The mean OCV of all the functioning fuel cells was 38.5 mV, with the rough-microstructure devices exhibiting a higher mean OCV of 44.7 mV (Figure 5b), than the dense membranes, which had a mean OCV of 34.5 mV (Figure 5b). In addition, the ratio of functioning devices for visually intact fuel-cell membranes was four times higher for the devices with the rough electrolyte microstructure (24 out of 30 devices functioning) than for the dense ones (60 out of 120 devices functioning). Here, we define a functioning device as a device with a non-zero OCV. These results provide a first indication that the rough microstructure reduces sources of lowered electrochemical potential as well as the total device failure rate. Sources for a reduced OCV can be electronic leakage through the ceria electrolyte, as dry (i.e., unprotonated) ceria with nanosized grains is a predominantly electronic conductor,[77] and it can be expected that some residual electronic conductivity is present in the hydrated case as well. In addition, the rough microstructure exhibits significantly lower stress (see the Supporting Information for optical microscopy images of buckling patterns), which reduces the chance of crack or pinhole formation[43] due to stress relief and, thus, the amount of electrode cross-talk. Finally, for the rough microstructure, we expected pinholes and nanoscale flaws to be more readily closed during the deposition process given the high degree of disorder in the thin film. However, no pinholes were visible using backlight microscopy in any of the devices with either microstructure tested here, and SEM could not be used for pin-hole analysis given the fragile nature of the glucose fuel cells when drawing a vacuum. It is worth noting the difference in quantity of 120 devices with dense microstructure compared to 30 devices with the rough electrolyte microstructure as potential source of statistical uncertainty of these results; however, it is also apparent that characterizing the OCV of 30 fuel cells in case of the rough electrolyte microstructure provides an unusually large sample size for first proof of concept experiments, providing confidence in the reproducibility of fuel cell performance demonstrated here. In total, 84 out of 150 glucose fuel cells were operational by exhibiting nonzero OCV, and we turn to cell testing of the total power output of a subset of these devices in the next step.

The power output performance of the glucose fuel cells with both rough and dense electrolyte microstructures were then characterized by measuring the current–voltage profiles (I–V curves) under 0.5 M glucose solution in PBS at the anode and air at the cathode. In total, 12 separate glucose fuel cells were measured (two with rough electrolyte microstructure and ten with dense electrolyte microstructure), with four voltage sweeps performed sequentially, over the course of up to 11 h per fuel cell. Figure 5d displays an example of a high-performing glucose fuel cell, which exhibited a peak power density of 43 $\mu W\ cm^{-2}$. We have recently shown that ceria exhibits slow hydration kinetics at room temperature;[76] therefore, careful equilibration is more important for ceria-based glucose fuel cells than for other systems such as Nafion-based glucose fuel cells. To balance the hydration kinetics considerations with surface degradation, measurements were taken after equilibration with pure water and then glucose solution for 12 h each. After this equilibration, the OCV of the particular device shown in Figure 5d, which had a dense ceria electrolyte microstructure, still increased over time despite equilibration over 24 h prior to the first measurement. This slow equilibration is important to consider for future implantation, as it implies that the device must be either preconditioned prior to implantation or will exhibit a transient time after initial implantation. Overall, the average peak power of all the measured devices was 11.4 $\mu W\ cm^{-2}$, indicating that the overall glucose-fuel-cell performance is competitive with that of other abiotic glucose fuel cells and that the power density reaches values that are relevant for miniaturized implantable devices (Figure 5e). The standard deviation of all 12 measured ceramic-electrolyte glucose fuel cells is 13 $\mu W\ cm^{-2}$, which corresponds to a significant scatter in performance data that remains to be fully explained, but is generally expected in the first proof of concept of a new electrochemical device. Table S6 (Supporting Information) shows the peak power density as well as key statistical parameters of all measured devices.

To use ceramic glucose fuel cells to power implantable biomedical devices, long-term stability is required to power devices such as sensors or neural stimulators. Therefore, it is worth emphasizing that the measurements of the I–V curves were obtained over the course of up to 11 h each, and multiple devices on the same chip were measured successfully, meaning that glucose fuel cells were exposed to glucose solution and characterized for up to 140 h. This observation is the first promising indication of the long-term stability of the solid-state micro-glucose-fuel-cells. After the longest measurement campaign of 140 h, we observed the formation of precipitates at the surface of the glucose- fuel-cell chip (see Figure S5, Supporting Information). These precipitates were organic salts, which likely formed from side reactions between glucose and dissolved species from the PBS. Overall, we observe strong fluctuations in both the OCV and power output data among the ceramic-electrolyte glucose fuel cells characterized here. This can be seen from the histograms in Figure 5a,b, and from the spread of peak power between 11.4 $\mu W\ cm^{-2}$ on average and 43 $\mu W\ cm^{-2}$ for the best-performing device. While the exact reasons for this strong fluctuation remain to be elucidated, it is to be expected that they stem primarily from the complex interaction

© 2022 The Authors. Advanced Materials published by Wiley-VCH GmbH

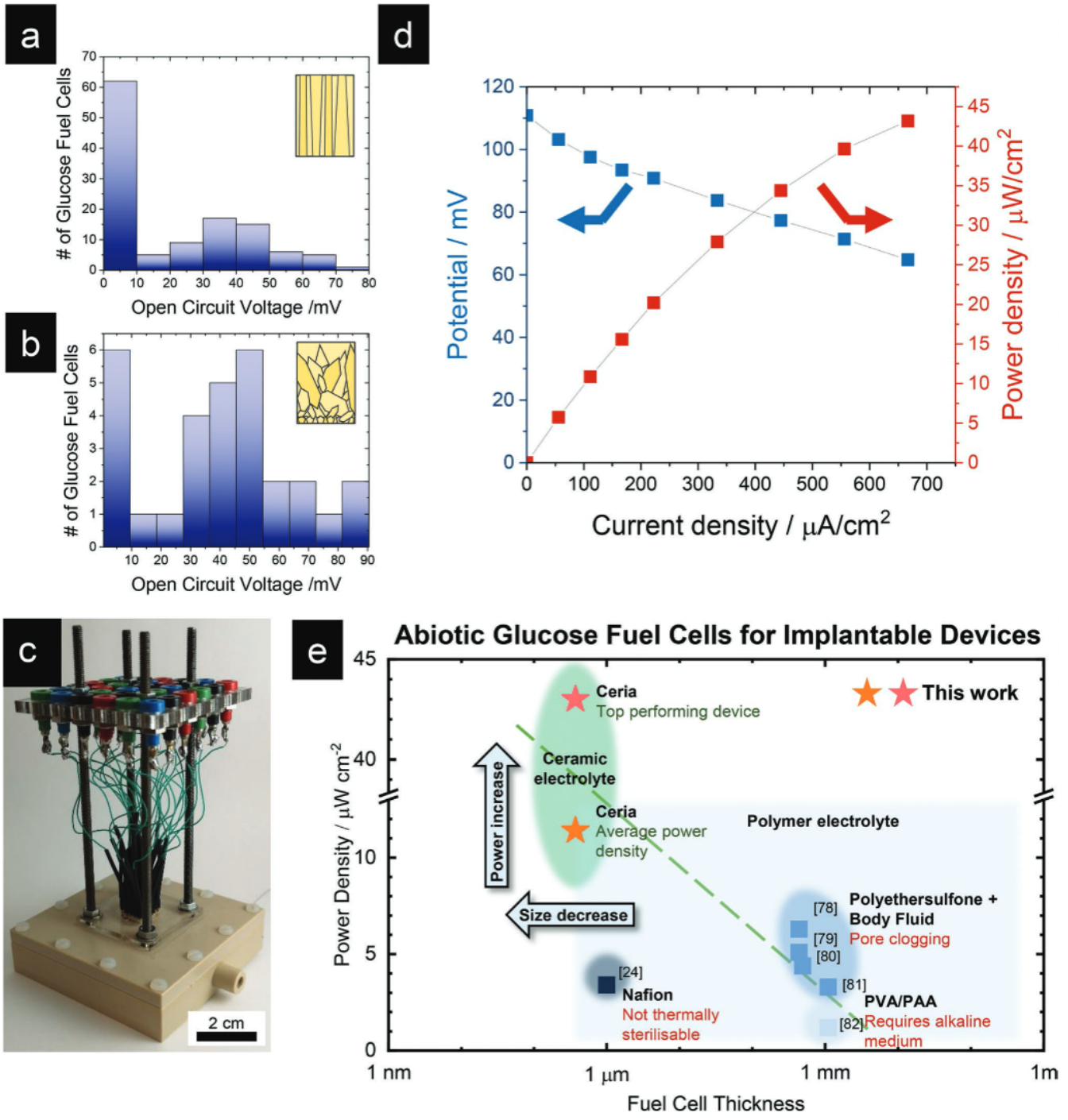

Figure 5. Performance and comparison of ceramic glucose fuel cells. a,b) Histograms of the open-circuit potentials of 120 ceramic glucose fuel cells with dense ceria electrolyte (a) and 30 ceramic glucose fuel cells with porous ceria electrolyte (b). c) Test setup allowing for rapid screening of 30 individual glucose-fuel-cell devices through spring-loaded needles and plug board. d) Polarization curve of a ceramic glucose fuel cell, exhibiting a peak power density of 43 μW cm^{-2}. e) Comparison of previously reported polymer-electrolyte-based glucose fuel cells[24,78–82] with those in this work, i.e., ceramic-electrolyte glucose fuel cells: power density as a function of fuel-cell thickness. The ceramic glucose fuel cells show three times higher miniaturization and higher power densities than existing abiotic glucose fuel cells.

between the slow hydration kinetics of ceria[76] with surface degradation and sluggish reaction kinetics of the electrode reactions at room temperature.

In conclusion, the ceramic glucose fuel cells presented here exhibited stable, high power densities at the highest degree of miniaturization reported to date. Figure 5e compares the power density and thickness of the fuel cells in this work with those of existing, lab-stage polymer-electrolyte glucose fuel cells. It can be seen that to date, there have been no abiotic polymer-electrolyte glucose fuel cells with form factors below

© 2022 The Authors. Advanced Materials published by Wiley-VCH GmbH

the micrometer scale. In addition, such polymer-electrolyte glucose fuel cells exhibit low steady-state power densities below 10 μW cm^{-2}.[24,78–82] In contrast, the ceramic glucose fuel cells reported here achieve competitive power densities, with that of the top-performing device reaching 43 μW cm^{-2}, and the average power density across 12 glucose fuel cells reaching 11.4 μW cm^{-2}. In addition, the thickness of the ceramic glucose fuel cell is three times thinner than the next-thinnest device, and ≈1000 times thinner than other abiotic glucose fuel cells reported to date. It is important to note that fuel-cell thickness directly translates into volumetric power density, implying that a thickness scale-down would not only reduce the device footprint for the patient but also allow for effective stacking to reach adequate total power levels. This is particularly important for implantable device applications, as it allows for ultrasmall power sources that enable the miniaturization of implants. Given the urgent need for miniaturized power sources for the practical realization of new biomedical implantable devices, this thickness scale-down has the potential to enable the development of an entire range of previously impossible implantable device technologies.

3. Conclusion

We have demonstrated the design and operation of a ceramic glucose fuel cell for implantable applications. Indeed, we were able to demonstrate that at body temperature, ceramic glucose fuel cells with proton-conducting ceria electrolyte films of less than 400 nm can deliver a peak power density of up to 43 μW cm^{-2}, albeit at elevated glucose concentrations. Being able to operate such ultrasmall ceramic-electrolyte glucose fuel cells using biocompatible and thermally sterilizable ceramics to harvest energy in the human body can become an enabler for future applications in electroceuticals, implantable sensing, and other bioelectronic devices. This sets ceramic glucose fuel cells apart from polymer-electrolyte glucose fuel cells. We confirmed the reproducible operation of these ceramic glucose fuel cells across 12 devices and presented OCV statistics across 150 different glucose fuel cells. The ceramic-electrolyte glucose fuel cell demonstrated here is fully fabricated on silicon using standard semiconductor microfabrication techniques, facilitating its integration into bioelectronic devices. In addition, its exclusive use of ceramic and noble metal materials enables simple thermal sterilization prior to implantation and promises long-term stability and overall robustness. In the future, in vivo studies will be required to verify the operation of the ceramic-electrolyte glucose fuel cell in a living organism. After the present initial proof-of-concept, it needs to be verified how the device operates as a single-chamber fuel cell implanted in a living organism, and in particular, the degradation of the glucose fuel cell within a body fluid such as interstitial fluid needs to be studied. En route to these in vivo studies, in vitro aging studies such as in the form of added hydrogen peroxide or potassium chloride can help elucidate the degradation behavior of the fuel cell system to prepare for future implantation. Excitingly, the present choice of materials can enable entirely new geometric layouts for the ceramic-electrolyte glucose fuel cell that will translate the demonstrated miniaturization to implant technology. In particular, the presented materials could be laid out in an in-plane architecture in the form of a coating with a thickness of ≈300 nm on the outside of the enclosure of an implantable device. In this design, the glucose fuel cell would essentially have no volumetric footprint, and inherit the mechanical robustness of the implantable device, enabling miniaturization of the whole implant to an unprecedented degree. It is noteworthy that the ceramic-electrolyte glucose fuel cell membranes demonstrated here are fragile due to their ultrathin nature, which is agreement with general trends in biomaterials that thin devices suffer in durability.[83] However, with potential designs such as the in-plane architecture previously mentioned, the ceramic-electrolyte glucose fuel cell is expected to be sufficiently mechanically robust for implantable applications. Beyond implantable applications, we have demonstrated that ceria films can be used as the electrolyte of room-temperature energy-conversion devices using through-plane proton conductivity, which could serve as a model for other small-scale low-temperature energy harvesters. Collectively, these ceramic glucose fuel cells constitute the smallest implantable power source to date and put new applications in highly miniaturized implantable devices into perspective.

4. Experimental Section

Overview: Micro-glucose-fuel-cells in the form of freestanding ceria membranes were designed and fabricated using ceramic thin films, metal sputtering, and a microfabrication route based on standard microfabrication techniques. Freestanding membranes were fabricated in the sequence of first creating freestanding Si_xN_y membranes integrated on silicon as a support for the subsequent deposition of a 250-nm layer of ceria as the proton-conducting electrolyte. The supporting layer of Si_xN_y was then removed, and metal electrodes were applied in a final step via magnetron sputtering. Here, a 100-nm nanoporous Pt electrode served as the anode, and a dense 20-nm Pt electrode served as the cathode. The entire fabrication process is schematically depicted in Figure S1 (Supporting Information).

Fuel-Cell Fabrication: Double-side-polished, ⟨100⟩ oriented 4 in. silicon wafers with thicknesses of 380 μm (Sil'tronix, France) served as the initial substrates for all the subsequent processing. The wafers were coated by the supplier with 200 nm of Si_xN_y on both sides using low-pressure chemical vapor deposition, resulting in low-stress films, which is a prerequisite for forming the freestanding ceramic membranes. The wafers were cut into square pieces measuring 22.3 mm × 22.3 mm using a dicing saw (DAD-3240, DISCO, Japan). After dicing, freestanding Si_xN_y membranes were fabricated as a support for the subsequent ceria membrane assembly. To create the freestanding Si_xN_y membranes, an etching mask of photoresist (AZ 5214, Merck KGaA, Germany) with 30 open squares was used as a template for the membranes, patterned via photolithography. The silicon nitride was locally removed inside these squares via reactive ion etching (Plasmatherm, USA), opening up square windows of pure silicon. The chips were then submerged into KOH solution (20 wt% in water, 80 °C; VWR International, USA) for anisotropic wet etching of silicon. This resulted in freestanding membranes of Si_xN_y, measuring 300 μm × 300 μm.

In the next step, the proton-conducting electrolyte was deposited as 250 ± 25 nm of pure cerium oxide for the fuel cells via pulsed laser deposition (PLD) on the silicon chip (PLD system by Surface Systems & Technology, Germany, equipped with a COHERENT COMPex Pro laser, wavelength 248 nm, USA). The ceria target was fabricated from commercial ceria powder (99.5% purity, Sigma Aldrich, USA) and

© 2022 The Authors. Advanced Materials published by Wiley-VCH GmbH

densified using the following procedure. The powder was first pressed uniaxially at 440 bar for 2 min and then pressed isostatically at 22 kbar for 2 min to form a dense pellet. The pellet was then sintered by heating to 1400 °C at a heating rate 3 °C min^{-1}, holding at 1400 °C for 4 h, and then cooling to room temperature at a cooling rate of 5 °C min^{-1}. The PLD deposition was performed at a distance of 75 mm, with a substrate temperature of 400 °C and a chamber pressure of 0.026 and 0.078 mbar of O_2. Two different microstructures of the ceria proton-conducting electrolyte were deposited via PLD. Dense ceria was deposited with 6100 shots at a laser fluence on the target of 1 J cm^{-2} and a laser repetition rate of 1 Hz. Rough ceria was deposited with 3000 shots at a laser fluence on the target of 2.75 J cm^{-2} and a laser repetition rate of 1 Hz.

Next, 100 ± 10 nm of porous Pt were deposited as the glucose-facing fuel-cell anode, which was deposited on top of the ceria thin film via reactive magnetron sputtering (Kurt J, Lesker, USA; Pt target: 99.99% purity, ACI Alloys). The deposition procedure for nanoporous Pt was adapted from a fabrication route previously reported by Jung et al.[71] Briefly, PtO_x was sputtered via DC magnetron sputtering under an oxygen-rich atmosphere (70% O_2 and 30% Ar, both ultra-high-purity grade, Airgas; chamber pressure 10 mTorr) and was subsequently thermally reduced via a heat-treatment process (400–600 °C) under Ar or 5% H_2 in Ar for 1–8 h. A shadow mask was used during the sputter deposition of the anode to pattern rectangular individual electrodes for each fuel cell, serving both as the electrodes and the current collectors.

The supporting layer of Si_xN_y was then removed via a second reactive-ion-etching step. Finally, 20 ± 2 nm of dense Pt was deposited on the backside of the chip as the oxygen-facing fuel-cell cathode, covering the entire backside without masking. The dense Pt cathode was deposited via DC magnetron sputtering at 10 mTorr Ar (ultrahigh purity grade, Airgas) using the same sputtering system and target as above.

Characterization and Measurements: OCV and current–voltage profiles of the fuel cells were measured using an electrochemical characterization system and the corresponding data collection software (VSP-300, BioLogic, France). XRD was performed on an X-ray diffractometer equipped with a 2D detector using Co Kα radiation at a voltage of 40 kV and current of 40 mA (D8 GADDS, Bruker, USA), and Raman spectroscopy was performed on a confocal Raman microscope (Alpha 300, WITec, Germany). SEM was performed on a field-emission scanning electron microscope (Ultra Plus, Zeiss, Germany). Electrochemical measurements were performed in a custom-designed case fabricated from PEEK and PMMA. The measurement enclosure was designed to enable the flexible and reproducible characterization of glucose-fuel-cell devices on chips containing 30 devices under controlled fuel supply in a two-chamber configuration. The case measures 80 mm × 80 mm with a thickness of 15 mm and contains a slot of 22.6 mm × 22.6 mm to hold the glucose-fuel-cell sample. The measurements were configured such that glucose solution (0.5 M in phosphate buffered saline solution, all from VWR International, USA) flows over the top side of the anode of the fuel-cell chip while the bottom is exposed to air, and both sides are tightly sealed using silicone paste (Baysilone, Bayer, Germany). Electrochemical measurements were performed using spring-loaded needles, with the case allowing rapid sequential measurement of all 30 glucose-fuel-cell devices housed on a single chip. Overall, this design enabled the measurement of the OCV of 150 glucose-fuel-cell devices and the current–voltage profiles of 12 fuel cells. Glucose solution was deaerated by bubbling N_2 (ultrahigh purity grade, Airgas, USA) through the solution for 24 h before any measurement. A peristaltic pump (Masterflex C/L 1–6 rpm, Masterflex, USA) was used to flow glucose solution over the glucose-fuel-cell chip at a flow rate of 150–300 µL min^{-1}. The glucose fuel cells were exposed to deionized water for 12 h and to deaerated glucose solution for an additional 12 h prior to any characterization of the OCV or *I–V* profile. All the water was Type 1 ultrapure water (MilliQ 8, Millipore, USA). Electrochemical impedance spectroscopy measurements were performed using a Zahner IM6 potentiostat (Zahner-elektrik, Germany) in the frequency range of 1 MHz to 100 mHz at a 50-mV amplitude, and the spectra were analyzed and fit using the software ZView (Scribner Associates, USA). Impedance measurements were performed in a controlled temperature and atmosphere chamber (Linkam Scientific, UK).

Statistical Analysis: The raw fuel-cell performance data in the form of chronopotentiometry for the OCV and multistep chronopotentiometry for the current–voltage profiles were processed in the following fashion: For OCV data, a custom software script in MATLAB (Mathworks, USA) was used to extract the OCV for each of the 30 glucose fuel cell devices per chip characterized, which were measured sequentially for 15 s each. This interval was deemed sufficiently long to assume equilibration, but short enough to ensure that all glucose fuel cell devices on the same chip had similar exposure times to the fuel solution. The campaign was repeated six times per chip, and for each individual device, the arithmetic mean was calculated. In total, $n_1 = 120$ glucose fuel cell devices on four chips, with the dense microstructure, and $n_2 = 30$ glucose fuel cell devices on one chip, with the rough microstructure, were characterized in this way. Here, n_i refers to the overall sample size of the experiment. The resulting mean OCVs were then aggregated in the form of histograms, representing the number of occurrences of certain voltage intervals among the n_1 and n_2 glucose fuel cell devices. Histograms were generated using the graphing and analysis software Origin (Originlabs, USA). Outliers, namely, nonfunctioning devices with an OCV of zero, were not removed from the histograms to represent the complete data and observe failure rates of devices.

For *I–V* profiles, raw data in the form of time-dependent current–voltage profiles were analyzed in similar fashion using a custom software script in MATLAB. By nature of the measurement, the current was always set by the electrochemical characterization system, and the voltages were extracted by calculating the arithmetic mean of the last 30 s of each current step which lasted 900 s for equilibration. In total $n_3 = 12$ glucose fuel cell devices were characterized for their current–voltage profiles. For each of these glucose fuel cells, four complete cycles of stepwise chronopotentiometry were performed. Given the observed transient nature of performance data, from these four cycles, the best performance was selected, as any poorer performance than the peak was attributed to either equilibration effects or degradation. In the body of the manuscript, the *I–V* curve of the best performing glucose fuel cell is shown, and the arithmetic mean and standard deviation of all $n_3 = 12$ devices is presented. Arithmetic mean and standard deviation were calculated using the software Excel (Microsoft, USA).

Supporting Information

Supporting Information is available from the Wiley Online Library or from the author.

Acknowledgements

The authors are grateful to Dr. Kun Joong Kim and Dr. Haemin Paik for the fruitful discussion of the experimental results and to Dr. Zachary Hood for support with microscopy. This work made use of the MRSEC Shared Experimental Facilities at MIT, supported by the National Science Foundation under Award No DMR-1419807. This work was performed in part at the Center for Nanoscale Systems (CNS), a member of the National Nanotechnology Coordinated Infrastructure Network (NNCI), which was supported by the National Science Foundation under NSF Award No. 1541959. CNS is part of Harvard University. P.S. gratefully acknowledges financial support through the Broshy Graduate Fellowship and Hugh Hampton Young Memorial Fund Fellowship at MIT and through Merck KGaA, Darmstadt, Germany. M.A.G. acknowledges financial support through the Zeno Karl Schindler Foundation, the Fondation Zdenek et Michaela Bakala, and the Swiss America Foundation. J.L.M.R. thanks the Thomas Lord Foundation for financial support.

© 2022 The Authors. Advanced Materials published by Wiley-VCH GmbH

Conflict of Interest

The authors declare no conflict of interest.

Author Contributions

P.S. and J.L.M.R. conceived the concept of the ceramic-based glucose micro-fuel-cell. P.S. designed the experimental apparatus and sample fabrication process. P.S., S.A.S., and M.A.G. fabricated the fuel cells, enhanced the characterization apparatus, and performed the electrochemical characterization. S.A.S. and L.F.O. performed post-mortem analyses. P.S. and J.L.M.R. wrote the manuscript, and all the authors reviewed and edited the final version of the manuscript.

Data Availability Statement

The data that support the findings of this study are available from the corresponding author upon reasonable request.

Keywords

bioelectronics, ceria, energy harvesting, glucose fuel cells, implantable devices

Received: November 9, 2021
Revised: March 21, 2022
Published online:

[1] "Electroceuticals/Bioelectric Medicine Market Size, Share & Analysis," https://www.reportsanddata.com/report-detail/electroceuticals-bioelectric-medicine-market (accessed: February 2021).
[2] K. Famm, B. Litt, K. J. Tracey, E. S. Boyden, M. Slaoui, *Nature* **2013**, *496*, 159.
[3] K. Birmingham, V. Gradinaru, P. Anikeeva, W. M. Grill, V. Pikov, B. McLaughlin, P. Pasricha, D. Weber, K. Ludwig, K. Famm, *Nat. Rev. Drug Discovery* **2014**, *13*, 399.
[4] H. G. Mond, G. Freitag, *PACE – Pacing Clin. Electrophysiol.* **2014**, *37*, 1728.
[5] A. Ben Amar, A. B. Kouki, H. Cao, *Sensors* **2015**, *15*, 28889.
[6] Y. Lee, D. Blaauw, D. Sylvester, *Proc. IEEE* **2016**, *104*, 1529.
[7] R. S. Sanders, in *Cardiac Pacing for the Clinician*, (Eds: F. M. Kusumoto, N. F. Goldschlager), Springer US, Boston, MA, USA **2008**, pp. 47–71.
[8] W. Greatbatch, J. H. Lee, W. Mathias, M. Eldridge, J. R. Moser, A. A. Schneider, *IEEE Trans. Biomed. Eng.* **1971**, *BME-18*, 317.
[9] D. C. Bock, A. C. Marschilok, K. J. Takeuchi, E. S. Takeuchi, *Electrochim. Acta* **2012**, *84*, 155.
[10] A. Kim, M. Ochoa, R. Rahimi, B. Ziaie, *IEEE Access* **2015**, *3*, 89.
[11] J. C. Schuder, *Artif. Organs* **2002**, *26*, 909.
[12] D. Seo, R. M. Neely, K. Shen, U. Singhal, E. Alon, J. M. Rabaey, J. M. Carmena, M. M. Maharbiz, *Neuron* **2016**, *91*, 529.
[13] Y. Zhu, J. C. Gonzalez-Rosillo, M. Balaish, Z. D. Hood, K. J. Kim, J. L. M. Rupp, *Nat. Rev. Mater.* **2021**, *6*, 313.
[14] S. Kerzenmacher, J. Ducrée, R. Zengerle, F. von Stetten, *J. Power Sources* **2008**, *182*, 1.
[15] D. Leech, P. Kavanagh, W. Schuhmann, *Electrochim. Acta* **2012**, *84*, 223.
[16] S. C. Barton, J. Gallaway, P. Atanassov, *Chem. Rev.* **2004**, *104*, 4867.
[17] R. Venkatasubramanian, C. Watkins, C. Caylor, G. Bulman, in *6th Int. Workshop on Micro and Nanotechnologies for Power Generation and Energy Conversion Applications (PowerMEMS 2006)*, Institute of Physics Publishing **2006**, p. 1.
[18] Y. Yang, X. J. Wei, J. Liu, *J. Phys. D: Appl. Phys.* **2007**, *40*, 5790.
[19] G. T. Hwang, H. Park, J. H. Lee, S. Oh, K. Il Park, M. Byun, H. Park, G. Ahn, C. K. Jeong, K. No, H. Kwon, S. G. Lee, B. Joung, K. J. Lee, *Adv. Mater.* **2014**, *26*, 4880.
[20] Z. Yang, S. Zhou, J. Zu, D. Inman, *Joule* **2018**, *2*, 642.
[21] Q. Zheng, B. Shi, F. Fan, X. Wang, L. Yan, W. Yuan, S. Wang, H. Liu, Z. Li, Z. L. Wang, *Adv. Mater.* **2014**, *26*, 5851.
[22] W. Jiang, H. Li, Z. Liu, Z. Z. Li, J. Tian, B. Shi, Y. Zou, H. Ouyang, C. Zhao, L. Zhao, R. Sun, H. Zheng, Y. Fan, Z. L. Wang, Z. Z. Li, *Adv. Mater.* **2018**, *30*, 1.
[23] R. C. Reid, S. D. Minteer, B. K. Gale, *Biosens. Bioelectron.* **2015**, *68*, 142.
[24] B. I. Rapoport, J. T. Kedzierski, R. Sarpeshkar, *PLoS One* **2012**, *7*, e38436.
[25] W. Greatbatch, C. F. Holmes, *IEEE Eng. Med. Biol. Mag.* **2002**, *10*, 38.
[26] J. O. M. Bockris, B. J. Piersma, E. Gileadi, *Electrochim. Acta* **1964**, *9*, 1329.
[27] A. T. Yahiro, S. M. Lee, D. O. Kimble, *Biochim. Biophys. Acta* **1964**, *88*, 375.
[28] J. T. Santini, M. J. Cima, R. Langer, *Nature* **1999**, *397*, 335.
[29] A. L. Benabid, P. Pollak, A. Louveau, S. Henry, J. de Rougemont, *Stereotact. Funct. Neurosurg.* **1987**, *50*, 344.
[30] J. Wessberg, C. R. Stambaugh, J. D. Kralik, P. D. Beck, M. Laubach, J. K. Chapin, J. Kim, S. J. Biggs, M. A. Srinivasan, M. A. L. Nicolelis, *Nature* **2000**, *408*, 361.
[31] Z. L. Wang, J. Song, *Science* **2006**, *312*, 242.
[32] F. R. Fan, Z. Q. Tian, Z. L. Wang, *Nano Energy* **2012**, *1*, 328.
[33] Ó. Santiago, E. Navarro, M. A. Raso, T. J. Leo, *Appl. Energy* **2016**, *179*, 497.
[34] V. Oncescu, D. Erickson, *Sci. Rep.* **2013**, *3*, 1226.
[35] S. Rengaraj, P. Kavanagh, D. Leech, *Biosens. Bioelectron.* **2011**, *30*, 294.
[36] Y. Sone, P. Ekdunge, D. Simonsson, *J. Electrochem. Soc.* **1996**, *143*, 1254.
[37] B. Smitha, S. Sridhar, A. A. Khan, *J. Membr. Sci.* **2005**, *259*, 10.
[38] M. S. A. Kamel, H. F. M. Mohamed, M. O. Abdel-Hamed, E. E. Abdel-Hady, *J. Solid State Electrochem.* **2019**, *23*, 2639.
[39] S. R. Samms, S. Wasmus, R. F. Savinell, *J. Electrochem. Soc.* **1996**, *143*, 1498.
[40] K. D. Kreuer, *J. Membr. Sci.* **2001**, *185*, 29.
[41] G. Alberti, M. Casciola, L. Massinelli, B. Bauer, *J. Membr. Sci.* **2001**, *185*, 73.
[42] J. P. Agalloco, J. E. Akers, R. E. Madsen, *PDA J. Pharm. Sci. Technol.* **1998**, 52.
[43] A. Evans, A. Bieberle-Hütter, J. L. M. M. Rupp, L. J. Gauckler, *J. Power Sources* **2009**, *194*, 119.
[44] Z. Shao, S. M. Haile, *Nature* **2010**, *3*, 255.
[45] E. D. Wachsman, K. T. Lee, *Science* **2011**, *334*, 935.
[46] D. J. L. Brett, A. Atkinson, N. P. Brandon, S. J. Skinner, *Chem. Soc. Rev.* **2008**, *37*, 1568.
[47] E. Fabbri, D. Pergolesi, E. Traversa, *Chem. Soc. Rev.* **2010**, *39*, 4355.
[48] S. Choi, C. J. Kucharczyk, Y. Liang, X. Zhang, I. Takeuchi, H. I. Ji, S. M. Haile, *Nat. Energy* **2018**, *3*, 202.
[49] S. Li, J. T. S. Irvine, *Solid State Ionics* **2021**, *361*, 115571.
[50] D. Pergolesi, E. Fabbri, A. D'Epifanio, E. Di Bartolomeo, A. Tebano, S. Sanna, S. Licoccia, G. Balestrino, E. Traversa, *Nat. Mater.* **2010**, *9*, 846.
[51] K. D. Kreuer, *Annu. Rev. Mater. Res.* **2003**, *33*, 333.
[52] H. G. Bohn, T. Schober, *J. Am. Ceram. Soc.* **2000**, *83*, 768.
[53] K. D. Kreuer, S. Adams, W. Münch, A. Fuchs, U. Klock, J. Maier, *Solid State Ionics* **2001**, *145*, 295.
[54] J. R. Brown, E. Mastromatteo, J. Horwood, *Am. Ind. Hyg. Assoc. J.* **1963**, *24*, 131.

© 2022 The Authors. Advanced Materials published by Wiley-VCH GmbH

[55] C. Walkey, S. Das, S. Seal, J. Erlichman, K. Heckman, L. Ghibelli, E. Traversa, J. F. McGinnis, W. T. Self, *Environ. Sci. Nano* **2015**, *2*, 33.
[56] C. Piconi, G. Maccauro, *Biomaterials* **1999**, *20*, 1.
[57] R. Manabe, S. Ø. Stub, T. Norby, Y. Sekine, *Solid State Commun.* **2018**, *270*, 45.
[58] M. Shirpour, G. Gregori, R. Merkle, J. Maier, *Phys. Chem. Chem. Phys.* **2011**, *13*, 937.
[59] G. Gregori, M. Shirpour, J. Maier, *Adv. Funct. Mater.* **2013**, *23*, 5861.
[60] T. S. Oh, D. A. Boyd, D. G. Goodwin, S. M. Haile, *Phys. Chem. Chem. Phys.* **2013**, *15*, 2466.
[61] C. Xu, X. Qu, *NPG Asia Mater.* **2014**, *6*, e90.
[62] Y. Shi, A. H. Bork, S. Schweiger, J. L. M. Rupp, *Nat. Mater.* **2015**, *14*, 721.
[63] V. Kumar, A. K. Abbas, N. Fausto, *Robbins and Cotran Pathologic Basis of Disease*, Elsevier Saunders, Philadelphia, PA, USA **2005**.
[64] D. G. Maggs, R. Jacob, F. Rife, R. Lange, P. Leone, M. J. During, W. V. Tamborlane, R. S. Sherwin, *J. Clin. Invest.* **1995**, *96*, 370.
[65] A. H. Ropper, M. A. Samuels, J. P. Klein, S. Prasad, *Adams and Victor's Principles of Neurology*, McGraw-Hill Education, New York **2019**.
[66] J. R. Rao, in *Bioelectrochemistry I. Biological Redox Reactions*, (Eds: G. Milazzo, M. Blank), Plenum, New York, **1983**, pp. 283–335.
[67] A. Infortuna, A. S. Harvey, L. J. Gauckler, *Adv. Funct. Mater.* **2008**, *18*, 127.
[68] R. Schmitt, A. Nenning, O. Kraynis, R. Korobko, A. I. Frenkel, I. Lubomirsky, S. M. Haile, J. L. M. Rupp, *Chem. Soc. Rev.* **2020**, *49*, 554.
[69] S. Kerzenmacher, M. Schroeder, R. Brämer, R. Zengerle, F. von Stetten, *J. Power Sources* **2010**, *195*, 6516.
[70] S. Kerzenmacher, U. Kräling, M. Schroeder, R. Brämer, R. Zengerle, F. von Stetten, *J. Power Sources* **2010**, *195*, 6524.
[71] W. Jung, J. J. Kim, H. L. Tuller, *J. Power Sources* **2015**, *275*, 860.
[72] J. L. M. Rupp, U. P. Muecke, P. C. Nalam, L. J. Gauckler, *J. Power Sources* **2010**, *195*, 2669.
[73] A. Bieberle-Hütter, P. Reinhard, J. L. M. Rupp, L. J. Gauckler, *J. Power Sources* **2011**, *196*, 6070.
[74] A. Kloke, C. Köhler, R. Gerwig, R. Zengerle, S. Kerzenmacher, *Adv. Mater.* **2012**, *24*, 2916.
[75] H. J. Avila-Paredes, C. T. Chen, S. Wang, R. A. De Souza, M. Martin, Z. Munir, S. Kim, *J. Mater. Chem.* **2010**, *20*, 10110.
[76] P. Simons, K. P. Torres, J. L. M. Rupp, *Adv. Funct. Mater.* **2021**, *31*, 2009630.
[77] A. Tschöpe, R. Birringer, *J. Electroceram.* **2001**, *7*, 169.
[78] C. Köhler, M. Frei, R. Zengerle, S. Kerzenmacher, *ChemElectroChem* **2014**, *1*, 1895.
[79] A. Kloke, C. Köhler, R. Zengerle, S. Kerzenmacher, *J. Phys. Chem. C* **2012**, *116*, 19689.
[80] S. Kerzenmacher, U. Kräling, T. Metz, R. Zengerle, F. von Stetten, *J. Power Sources* **2011**, *196*, 1264.
[81] S. Kerzenmacher, J. Ducrée, R. Zengerle, F. von Stetten, *J. Power Sources* **2008**, *182*, 66.
[82] S. Ghaffari, M. R. Mousavi, M. Salehieh, *Proc. – Int. Conf. Intell. Syst. Model. Simul., ISMS* **2013**, 148.
[83] A. J. T. Teo, A. Mishra, I. Park, Y.-J. Kim, W.-T. Park, Y.-J. Yoon, *ACS Biomater. Sci. Eng.* **2016**, *2*, 454.

© 2022 The Authors. Advanced Materials published by Wiley-VCH GmbH